NAR Cancer, 2024, **6**, zcae021
https://doi.org/10.1093/narcan/zcae021
Advance access publication date: 20 May 2024
Cancer Gene Regulation, Chromatin, and Epigenetics

OXFORD

FBXO42 activity is required to prevent mitotic arrest, spindle assembly checkpoint activation and lethality in glioblastoma and other cancers

Pia Hoellerbauer[1,2], Megan Kufeld[1], Sonali Arora[1], Kelly Mitchell[1], Emily J. Girard[3,4], Jacob A. Herman[1], James M. Olson[3,4] and Patrick J. Paddison[1,2,*]

[1]Human Biology Division, Fred Hutchinson Cancer Center, Seattle, WA, 98109 USA
[2]Molecular and Cellular Biology Program, University of Washington, Seattle, WA, 98109 USA
[3]Clinical Research Division, Fred Hutchinson Cancer Center, Seattle, WA, 98109 USA
[4]Ben Towne Center for Childhood Cancer Research, Seattle Children's Research Institute, Seattle, WA, 98101 USA

[*]To whom correspondence should be addressed. Email: paddison@fredhutch.org

Abstract

Glioblastoma (GBM) is the most common and aggressive brain tumor in adults. To identify genes differentially required for the viability of GBM stem-like cells (GSCs), we performed functional genomic lethality screens comparing GSCs and control human neural stem cells. Among top-scoring hits in a subset of GBM cells was the F-box-containing gene *FBXO42*, which was also predicted to be essential in ∼15% of cell lines derived from a broad range of cancers. Mechanistic studies revealed that, in sensitive cells, *FBXO42* activity prevents chromosome alignment defects, mitotic cell cycle arrest and cell death. The cell cycle arrest, but not the cell death, triggered by *FBXO42* inactivation could be suppressed by brief exposure to a chemical inhibitor of Mps1, a key spindle assembly checkpoint (SAC) kinase. *FBXO42*'s cancer-essential function requires its F-box and Kelch domains, which are necessary for FBXO42's substrate recognition and targeting by SCF (SKP1–CUL1–F-box protein) ubiquitin ligase complex. However, none of FBXO42's previously proposed targets, including ING4, p53 and RBPJ, were responsible for the observed phenotypes. Instead, our results suggest that FBOX42 alters the activity of one or more proteins that perturb chromosome–microtubule dynamics in cancer cells, which in turn leads to induction of the SAC and cell death.

Graphical abstract

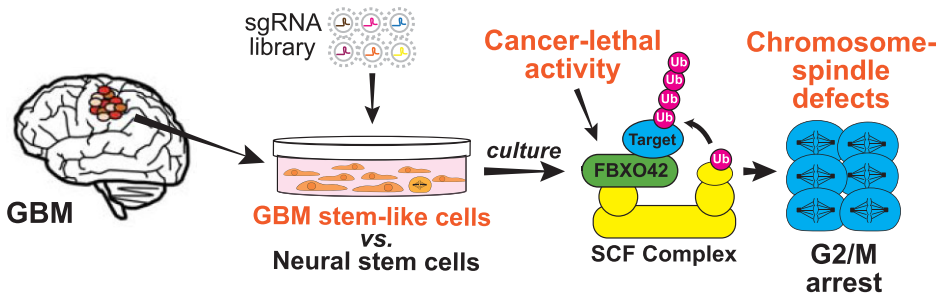

Introduction

Gliomas account for ∼30% of all central nervous system tumors (1). The most aggressive and common form is glioblastoma (GBM) (2). There are currently no highly effective therapies against GBM. With standard-of-care (SOC) treatments, consisting of surgery, radiation and the alkylating agent temozolomide (TMZ), ∼90% of adult patients die within 2 years of diagnosis (3,4). The median survival for GBM patients overall ranges from 14 to 17 months, with rare exceptions of long-term survival (5,6).

Although SOC effectively 'debulks' GBM tumors, it does not prevent tumor regrowth and disease recurrence, resulting in the observed modest survival benefits. The prevailing rationale is that tumors harbor slow-dividing GBM stem-like cells (GSCs), which are both missed by surgery and SOC resistant and cause tumor regrowth (7–9). This concept was elegantly demonstrated in a mouse model of glioma where a quiescent subset of endogenous glioma cells was shown to be responsible for tumor regrowth after TMZ treatment (10).

For modeling of human GBM, culture methods have been established that allow expansion of tumor samples in serum-free conditions that allow retention of many of the properties and molecular features associated with patient tumor isolate, including stem-like cell states, gene expression states and DNA alterations (7–9,11). We and others have previously used human GSCs, grown in these conditions (i.e. EGF,

Received: March 12, 2024. **Revised:** April 23, 2024. **Editorial Decision:** April 25, 2024. **Accepted:** May 15, 2024

FGF2 and N2B27 supplemented media on laminin-coated plates), as models for identifying cancer-specific molecular vulnerabilities in the context of functional genomic or small molecular inhibitor screens (12–18). Since these same culture conditions also allow for expansion of untransformed human neural stem cells (NSCs), GSCs and NSCs can be directly compared and vulnerabilities can be arguably defined as tumor specific.

This approach has led to discovery of multiple tumor-specific gene dependencies affecting the regulation of chromosome–microtubule associations [e.g. defects in chromosome congression (*ZNF207/BuGZ*) (15) and stable end on attachment of kinetochores (*BUB1B/BubR1*) (12,13,19)], the integrity of centrosome function (*ZNF131*) (17), the maintenance of exon recognition (*PHF5A*) (14) and regulation of entry into mitosis (e.g. via inhibitory phosphorylation of CDK1) (*PKMYT1*) (16). Many of these dependencies arise from misregulation of oncogenic signaling pathways and/or activity of specific oncogenes (e.g. MYC and transcriptional amplification).

Here, we characterize another cancer-specific hit defined from CRISPR–Cas9 lethality screens performed in GSCs and NSCs: *FBXO42*, which encodes a little studied F-box protein that serves as the substrate-recognition component of an SCF (SKP1–CUL1–F-box protein)-type E3 ubiquitin ligase complex (20–23). FBXO42 has been proposed to target and regulate p53 stability in osteosarcoma cells, an activity that could potentially broadly impact p53 wild-type (wt) cancers (21) and be linked to chromosome–spindle dynamics in HAP1 cells (24). Here, we define viability requirement for *FBXO42* in a subset of GBM isolates and also other cancer cell lines. We find that *FBXO42* promotes chromosome congression and spindle attachment, preventing mitotic arrest and spindle assembly checkpoint (SAC) activation, loss of cell viability and loss of tumor maintenance. However, we observe that *FBXO42* requirement is independent of p53 and its two other known substrates, ING4 and RBPJ. Possible mechanisms and candidate substrates are discussed.

Materials and methods

Key reagents and resources are available in Supplementary Table S3.

Ethical statement

We followed the guidelines set by the Fred Hutchinson Cancer Center Institutional Review Office for De-identified Human Specimens and/or Data, which categorizes the studies presented here as 'Research Not Involving Human Subjects' as detailed by the Institutional Review Board's Human Subjects Research Determination Form.

Cell culture

Isolates were cultured in NeuroCult NS-A basal medium (StemCell Technologies) supplemented with B27 (Thermo Fisher Scientific), N2 [homemade 2× stock in Advanced DMEM/F-12 (Thermo Fisher Scientific)], EGF and FGF-2 (20 ng/ml) (PeproTech), GlutaMAX (Thermo Fisher Scientific) and antibiotic–antimycotic (Thermo Fisher Scientific). Cells were cultured on laminin (Trevigen or in-house-purified)-coated polystyrene plates and passaged as previously described (11), using Accutase (EMD Millipore) to detach cells.

Lentivirus production

For virus production, lentiCRISPR v2 plasmids (25) were transfected using polyethylenimine (Polysciences) into 293T cells along with psPAX and pMD2.G packaging plasmids (Addgene) to produce lentivirus. For the whole-genome CRISPR–Cas9 libraries, 25 × 150 mm plates of 293T cells were seeded at ∼15 million cells per plate. Fresh medium was added 24 h later and viral supernatant harvested 24 and 48 h after that. For screening, virus was concentrated 1000× following ultracentrifugation at 6800 × *g* for 20 h. For validation, lentivirus was used unconcentrated at a multiplicity of infection of <1.

CRISPR–Cas9 screening

For screening, cells were transduced to achieve ∼750× representation of the library (at ∼30% infection efficiency to ensure a high proportion of single integrants). Two days after transduction, medium was replaced with medium containing 2 μg/ml puromycin. After 3 days of selection, portions of cells representing 500–750× coverage of the library were collected as the 'Day_0' samples. The remaining cells were cultured and consistently maintained at 500–750× representation for 21–23 days, after which time the 'Day_final' samples were collected. Screening was carried out in triplicate. To read out screen results, genomic DNA was extracted using the QIAamp DNA Blood Mini Kit (QIAGEN), and a two-step polymerase chain reaction (PCR) procedure was used to first amplify the genomically integrated single-guide RNA (sgRNA) sequences and then incorporate Illumina deep sequencing adapters and barcodes onto the sgRNA amplicons. For the first round of PCR, a sufficient number of PCR reactions were carried out to use all gDNA from the 500–750× coverage sample of cells at 2 μg genomic DNA per PCR reaction, using MagniTaq Multiplex PCR Master Mix (Affymetrix) and 12 cycles. For the second round of PCR, 5 μl of the first-round product was used as a template in combination with primers that would add the deep sequencing adapters and barcodes, using Herculase II Fusion DNA Polymerase (Agilent) and 16 cycles. Amplicons from the second-round PCR were then column purified using the PureLink Quick PCR Purification Kit (Invitrogen). Purified PCR products were sequenced using HiSeq 2500 (Illumina). Bowtie (26) was used to align the sequenced reads to the sgRNA library, allowing for one mismatch. The R/Bioconductor package edgeR (27) was used to assess changes across groups.

RNA-seq analysis

Cells were lysed with TRIzol (Thermo Fisher). Total RNA was isolated (Direct-zol RNA Kit, Zymo Research) and quality validated on the Agilent 2200 TapeStation. Illumina sequencing libraries were generated with the KAPA Biosystems Stranded RNA-Seq Kit and sequenced using HiSeq 2000 (Illumina) with 100-bp paired-end reads. RNA-seq reads were aligned to the UCSC hg19 assembly using STAR2 (v. 2.6.1) (28) and counted for gene associations against the UCSC gene database with HTSeq (29). Normalized gene count data were used for subsequent hierarchical clustering [R package ggplot2 (30)] and differential gene expression analysis [R/Bioconductor package edgeR (27)]. Heatmaps were made using R package pheatmap (31).

Western blotting

Cells were harvested, washed with phosphate-buffered saline (PBS) and lysed with modified RIPA buffer [150 mM NaCl, 25 mM Tris–HCl (pH 8.0), 1 mM ethylenediaminetetraacetic acid (EDTA), 1.0% Igepal CA-630 (NP-40), 0.5% sodium deoxycholate, 0.1% sodium dodecyl sulfate, 1× protease inhibitor cocktail (cOmplete Mini EDTA-free, Roche)]. Lysates were sonicated (Bioruptor, Diagenode) and then quantified using Pierce BCA assay (Thermo Fisher). Identical amounts of proteins (20–40 μg) were electrophoresed on 4–15% Mini-PROTEAN TGX precast protein gels (Bio-Rad). For transfer, the Trans-Blot Turbo transfer system (Bio-Rad) with nitrocellulose membranes was used according to the manufacturer's instructions. TBS (137 mM NaCl, 20 mM Tris, pH 7.6) + 5% nonfat milk was used for blocking, and TBS + 0.1% Tween 20 + 5% milk was used for antibody incubations. The following commercial primary antibodies were used: MX1 (Cell Signaling Technologies, #37849S, 1:500), Tp53 (Cell Signaling Technologies, #48818, 1:500), α-Tubulin (Sigma, #T9026, 1:1000) and β-Actin (Cell Signaling Technologies, #3700S, 1:2000). The following secondary antibodies were used (LI-COR, all 1:10 000): #926-68073, #926-32212, #926-32214, #926-68074, #925-32212 and #925-68071. An Odyssey infrared imaging system (LI-COR) was used to visualize blots.

Cas9:sgRNA RNP nucleofection

To prepare ribonucleoprotein (RNP) complexes, reconstituted sgRNA (Synthego) and then sNLS-SpCas9-sNLS (Aldevron) were added to complete SG Cell Line Nucleofector Solution (Lonza), to a final volume of 20 μl. The mixture was incubated at room temperature for 15 min to allow RNP complexes to form. A Cas9:sgRNA molar ratio of 1:2 was used, unless otherwise noted. Total RNP doses described refer to the amount of the limiting complex member (Cas9). To nucleofect, 1.5×10^5 cells were harvested, washed with PBS, resuspended in 20 μl of RNPs and electroporated using the Amaxa 96-well Shuttle System or 4D X Unit (Lonza) and program EN-138.

CRISPR editing analysis

Nucleofected cells were harvested at indicated time points and genomic DNA was extracted (MicroElute Genomic DNA Kit, Omega Bio-Tek). Genomic regions around CRISPR target sites were PCR amplified using Phusion polymerase (Thermo Fisher Scientific) and primers located (whenever possible) at least 250 bp outside sgRNA cut sites. After size verification by agaorse gel electrophoresis, PCR products were column purified (Monarch PCR & DNA Clean-up Kit, New England Biolabs) and submitted for Sanger sequencing (Genewiz) using unique sequencing primers. The resulting trace files for edited cells versus control cells (nucleofected with nontargeting Cas9:sgRNA RNPs) were analyzed for predicted indel composition using the Inference of CRISPR Edits web tool (32). See detailed CRISPR RNP nucleofection protocol in Supplementary data for general PCR conditions used for Phusion polymerase. See Supplementary Table S3 for a list of all PCR and sequencing primers used, as well as PCR conditions specific to particular genomic regions.

Flow cytometry

For cell cycle analysis and phospho-H3 quantification, cells were resuspended in PBS and dropwise fixed with 100% ethanol (resulting in final concentration of 70% ethanol). Samples were left in ethanol at 4°C overnight and then washed with cold PBS + 2% bovine serum albumin (BSA) and stained for 30 min at 4°C with cold PBS + 2% BSA + 0.1% (v/v) Triton X-100 + 1 μg/ml DAPI + AF488-conjugated phosphohistone H3 (Ser10) antibody (1:100, Cell Signaling Technologies, #3465S). Cells were then washed with and finally resuspended in cold PBS + 2% BSA. Processed cells were analyzed immediately by flow cytometry using either a BD FACSymphony A5 or BD LSRFortessa X-50 machine, using UV light excitation at 340–380 nm for DAPI and detection of DAPI emission at blue wavelengths (bandpass at 470 ± 20 nm). A pulse width–pulse area signal was used to discriminate G2/M cells from cell doublets and gate out the latter. Results were analyzed using FlowJo software, with the built-in Dean–Jett–Fox model used for cell cycle analysis.

Viability assays

For viability assays on gene knockouts, cells were given 2–3 days to recover from CRISPR nucleofection. Cells were then counted (NucleoCounter, NBS) and equal numbers were seeded in triplicate into 96-well plates at various dilutions to allow for multiple time points to be assessed. Cells were fed with fresh medium every 2–3 days. Relative viable cell numbers were measured using CellTiter-Glo Luminescent Cell Viability Assay (Promega) according to manufacturer's instructions. Briefly, medium on the cells was removed and replaced with 100 μl/well PBS, followed by addition of 100 μl/well CellTiter-Glo reagent. Plates were placed on a plate shaker for 5 min followed by incubation at room temperature for 10 min. Samples were then transferred to white-walled and white-bottom plates (150 μl/well) and luminescence was measured using an integration time of 0.25 s.

Time-lapse microscopy

Cells were first infected with lentivirus for PGK-H2B-EGFP (Addgene) and then nucleofected with CRISPR RNPs as needed and plated into 24-well or 12-well plates. One to three days post-nucleofection (depending on cell line and onset of gene knockout phenotype), cells were placed into an IncuCyte S3 (Sartorius) instrument. For the mitotic transit time analysis, phase and fluorescence (GFP) images were taken every 5 min for 48–72 h. Videos were compiled using the IncuCyte S3 software, and mitotic transit time was then analyzed for individual cells. A cell was considered to enter mitosis when nuclear envelope breakdown was evident based on EGFP visualization and when a visible morphology change from flat to round was observed. Following successful cytokinesis (proper cytoplasmic division resulting in two daughter cells), a cell was categorized as having successfully completed mitosis. A cell was classified as cytokinesis failure if the cell failed to divide following mitotic entry due to an abrupt mitotic exit while in metaphase or anaphase, or failure to complete cytokinesis. If a cell seemed to experience cytokinesis failure, it was followed for additional time to ensure that this was indeed the case. A cell was categorized as cell death in mitosis if a cell erupted and died during mitosis (between nuclear envelope breakdown and cytokinesis).

Generation of Dox-inducible FBXO42 cells

We cloned an *sgFBXO42_1*-resistant version of the *FBXO42* open reading frame (ORF) into the retroviral Tet-On vector pTURN-tight and transduced GSC-0827 cells with virus for this construct. Keeping the cells on doxycycline (Dox) to maintain exogenous *FBXO42* expression, we then nucleofected them with CRISPR RNPs for sgFBXO42_1 in order to knock out the endogenous *FBXO42* alleles. To obtain cells with a uniform and well-controllable induction of exogenous expression, we then derived clones from this cell pool. We screened the clones for proper ability to turn off the construct by taking a subset of cells of each clone and testing for viability loss upon Dox removal. Based on these results, we took our top two clones (clones 6 and 15), PCR amplified the endogenous FBXO42 locus and sequenced individual alleles using a TA cloning-like method.

Xenograft tumors

All *in vivo* experiments were conducted in accordance with the NIH Guide for the Care and Use of Experimental Animals and with approval from the Fred Hutchinson Cancer Research Center, Institutional Animal Care and Use Committee (Protocol 1457). One hundred thousand GSCs were orthotopically xenografted into a single frontal cerebral hemisphere or in flanks of HSD:athymic nude Foxn1nu mice (#069, Envigo). For Dox-FBXO42 experiments, 2 days prior to tumor cell implant, 2 mg/ml Dox with 5% sucrose (w/v) was added to the mouse drinking water.

Results

CRISPR–Cas9 screen identifies *FBXO42* as a selective lethal gene in a subset of GSC isolates

We previously performed genome-scale CRISPR–Cas9 lethality screens in two adult human GSCs (GSC-0131, mesenchymal; GSC-0827, proneural) and two human NSC isolates (CB660 and U5) to identify genes differentially required for GSC outgrowth isolates (16) (Figure 1A). Among the strongest GSC selective hit screens was *FBXO42*, which scored as essential in GSC-0827 cells, but was seemingly completely dispensable in GSC-0131, GSC-1502 and NSCs. As mentioned above, *FBXO42* encodes an F-box protein that serves as the substrate-recognition component of an SCF-type E3 ubiquitin ligase complex (20–23), which has been implicated in destabilizing p53, similarly to MDM2 (21). GSC-0827 cells are p53wt, while GSC-0131 and GSC-1502 are p53mut. Thus, we wondered whether *TP53* status might explain *FBXO42*'s GSC-0827-specific requirement and, therefore, decided to explore this screen hit further.

First, we performed a retest screen among multiple GSC isolates and found one additional GSC isolate that showed requirement for *FBXO42* (Figure 1B and Supplementary Table S1). Given this seemingly low percentage, we next explored requirement among a broad sampling of cancer cell lines using data now available through the Broad and Sanger Institutes (33,34). This included the use of cell line gene effect scores or CERES scores from CRISPR–Cas9, where *FBXO42* was included as a target (33) (Figure 1C). Using a cutoff of −0.5, we observed that cancer cell lines from most tissue lineages contain a subset of *FBXO42* loss-sensitive (F42L-*S*) cell lines, with a range of 0–30%, a mean of 13.2% and a median of 11.1% (Figure 1C). Across all tissues, ∼15% of cell lines were predicted to be potentially F42L-*S*, in line with the frequency we observed for GSC isolates.

To substantiate these findings further, we performed individual retests using an optimized method for nucleofection of sgRNA:Cas9 RNP complexes (35). We nucleofected GSC-0827 and NSC-U5 with CRISPR RNPs targeting *FBXO42*, *HEATR1* (an essential gene control) and *CD8A* (a nonessential gene targeting control) and measured relative cell viability. We found that loss of *FBXO42* did indeed have a profound effect on F42L-*S* GSC-0827 cells ($P < 0.01$), scoring similarly to *HEATR1* ($P < 0.01$) with almost no cells surviving, but did not negatively affect predicted F42L-*R* GSC-0131 and NSC-U5 cells (Figure 1D). Importantly, we observed a strong reduction in viability in NSC-U5 when targeting *HEATR1* ($P < 0.01$), indicating that our differential results were not due to reduced nucleofection efficiency in GSC-0131 and NSC-U5 cells.

We also examined the predicted F42L-*S* cell lines from Figure 1C. We picked four F42L-*S* cell lines—the breast cancer ductal carcinoma line BT549, the osteosarcoma line 143B, the GBM line T98G and the gastric adenosquamous carcinoma line MKN1—and nucleofected RNPs as above. These four lines showed exquisite (approximately similar to *HEATR1* loss) or moderate (significant but less than *HEATR1* loss) F42L sensitivity (Figure 1E). Taken together, the results suggest the F42L-*S* phenotype is applicable to a significant subset of cancers arising from a broad range of tissues.

FBXO42's substrate recognition and SCF interaction domains are required for viability in F42L-*S* cells but not its known substrates

Since FBXO42 is an F-box-containing protein that serves as the substrate-recognition component of an SCF-type E3 ubiquitin ligase complex (36), we hypothesized that failure to degrade one or more of its substrates after loss of *FBOX42* results in the F42L-*S* phenotype. Knowledge of the functional domains of FBXO42 allowed us to test the general hypothesis that its participation in an E3 ligase complex is essential for maintaining viability in F42L-*S* cells.

F-box proteins interact with SKP1 through their F-box domain, while they interact with ubiquitination targets through other protein interaction domains. Besides an F-box domain, FBXO42 additionally contains solely a Kelch repeat domain (37), which serves as its substrate-binding domain (20,21,23,37). Therefore, we created lentiviral constructs containing 3XFLAG-tagged ΔF-box domain (deletion of amino acids 39–93) and ΔKelch domain (deletion of amino acids 107–354) mutant versions of *FBXO42*, along with a 3XFLAG-tagged full-length *FBXO42* control construct. We then transduced GSC-0827 cells with these constructs, which also conferred puromycin resistance, and selected them with puromycin. In order to test whether exogenous expression of the full-length, ΔF-box and ΔKelch versions was able to rescue loss of endogenous *FBXO42*, we nucleofected the cells with CRISPR RNPs for two *FBXO42* sgRNAs to which the lentiviral vectors had been designed to be resistant (via synonymous mutation of multiple bases and use of an sgRNA spanning an intron–exon boundary), along with nontargeting and targeting control sgRNAs, and subsequently measured relative cell viability (Figure 2A). We observed that relative to the sgCD8A targeting controls, expression of full-length *FBXO42* was able to almost fully rescue the viability loss

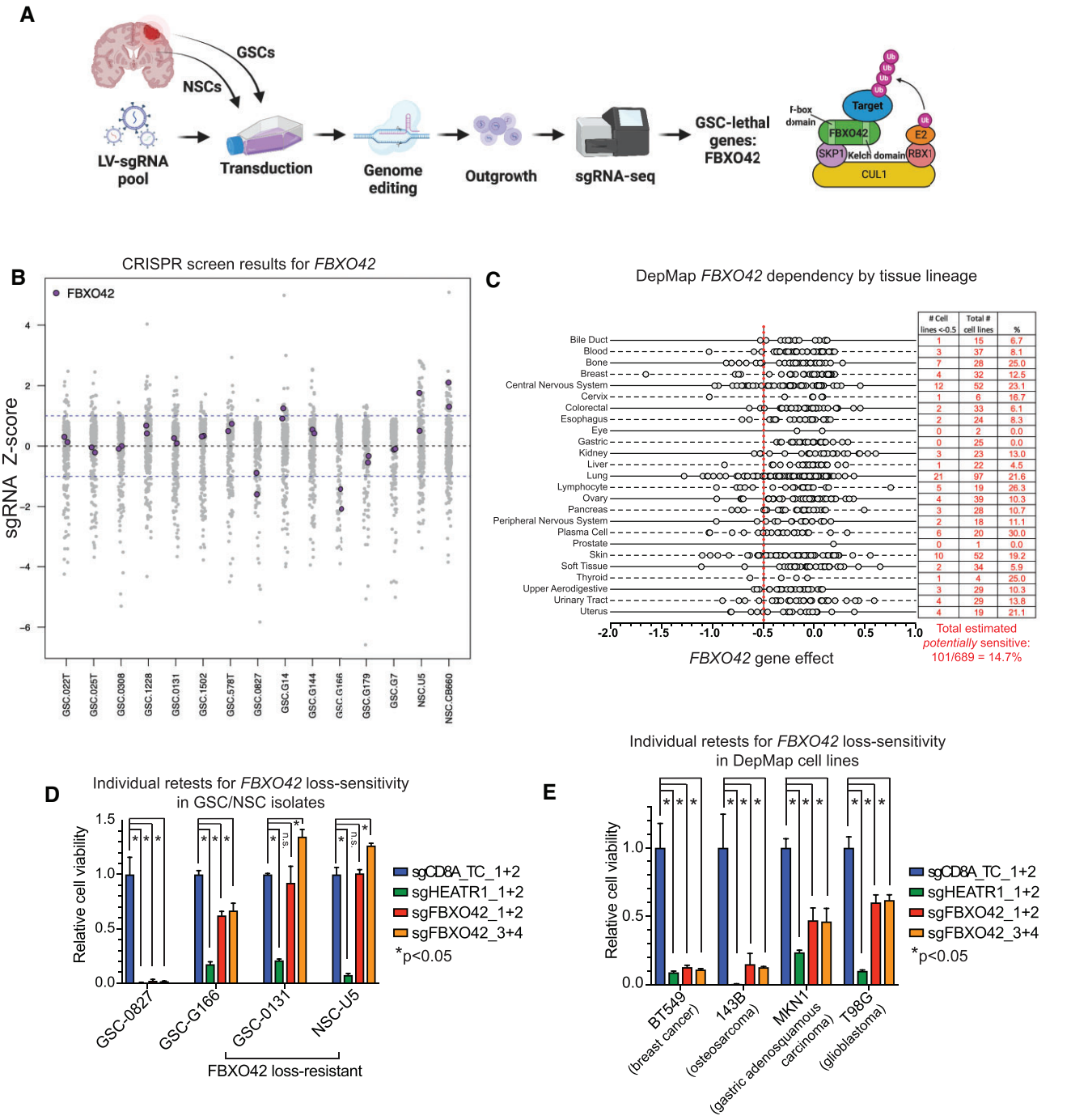

Figure 1. Identification of *FBXO42* as a candidate cancer-lethal gene. (**A**) Overview of functional genomic screens that revealed *FBXO42* as a candidate GBM-lethal gene. (**B**) Retest screens of GSC-specific hits from (16), showing how sgRNAs targeting *FBXO42* scored. Cells were infected with LV-Cas9-sgRNA pool, outgrown for 21 days and subjected to sgRNA-seq (made in part using BioRender). (**C**) Breakdown by tissue lineage of *FBXO42* dependency in cell lines screened in DepMap (CERES score from CRISPR Avana 19Q4 dataset). Each circle corresponds to a cell line. Summary of proportion of potentially sensitive cell lines (score <-0.5) by tissue lineage is shown to the right. (**D**) Relative cell viability (normalized to targeting control *sgCD8A*) for GSCs and NSCs nucleofected with CRISPR RNPs targeting *FBXO42*. *HEATR1* is an essential control gene. *sgTC = CD8A* targeting control sgRNAs. Measured at 9 days post-nucleofection for GSCs and 11 days for NSCs (due to doubling time differences) ($n = 3$; $^{*}P_{val} < 0.01$, Student's *t*-test). Cutting efficiencies of FBXO42 sgRNAs are shown in Supplementary Figure S1. (**E**) Relative cell viability (normalized to targeting control *sgCD8A*) for four cell lines that were nucleofected with CRISPR RNPs targeting *FBXO42*. Lines had been predicted *FBXO42* loss-sensitive based on DepMap data (using CRISPR Avana dataset for all except MKN1, which were predicted based on combined RNA interference dataset). *HEATR1* is an essential control gene. *sgTC = CD8A* targeting control sgRNAs. Measured at 8–12 days post-nucleofection (depending on doubling time) ($n = 3$; $^{*}P_{val} < 0.01$, Student's *t*-test).

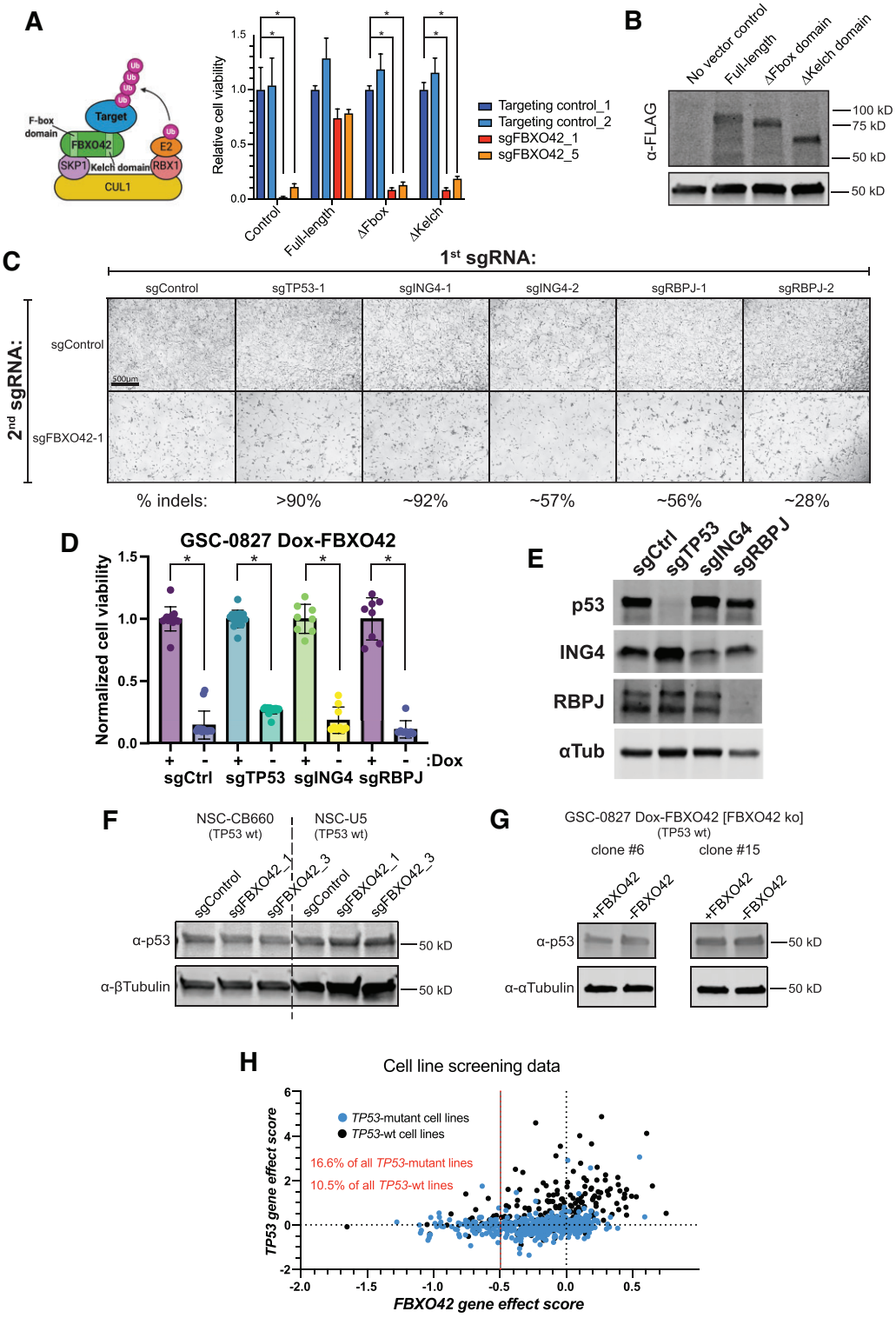

Figure 2. *FBXO42*'s ubiquitin ligase activity-associated domains are required in FBXO42-sensitive cells, but not its known targets. (**A**) Relative cell viability (normalized to targeting control *sgCD8A*) for GSC-0827 transduced with full-length, F-box domain deletion mutant or Kelch domain deletion mutant versions of 3XFLAG-*FBXO42* and then nucleofected with CRISPR RNPs targeting *FBXO42*, measured at 8 days post-nucleofection. The lentiviral expression constructs are resistant to the *FBXO42* sgRNAs used here. Untransduced GSC-0827 is shown for comparison. Targeting control = CD8A sgRNAs ($n = 3$; $^{*}P_{val} < 0.01$, Student's *t*-test). (**B**) Western blot for FLAG tag in transduced GSC-0827 used for viability assay in panel (A). (**C**) Representative images of GSC-0827 nucleofected with CRISPR RNPs targeting the published FBXO42 targets/interactors TP53, ING4 or RBPJ in combination with *sgNTC* or *sgFBXO42*, taken at 5 days post-nucleofection. (**D**) Normalized cell viability of GSC-0827 Dox-FBOX42 clone 15 cells 6 days after Dox+/− and nucleofection of pooled sgRNAs from panel (D) as shown [$n = 8$ (four replicates from two separate nucleofections performed on different days); $^{*}P_{val} < 0.01$, Student's *t*-test]. (**E**) Western blot results from nucleofections performed in parallel from panel (D). (**F, G**) Western blots for p53 levels in NSCs nucleofected with CRISPR RNPs targeting *FBXO42* and GSC-0827 clones 6 and 15, 4 days after Dox removal. (**H**) Cell line functional genomic screening data from DepMap showing *FBXO42* dependency score versus *TP53* dependency score (CERES scores from CRISPR Avana 19Q4 dataset). *TP53*-mutant cell lines are marked in blue.

observed upon endogenous *FBXO42* knockout. However, with expression of the ΔF-box and ΔKelch versions, we observed a similar viability loss upon *FBXO42* knockout as we observed in untransduced control GSC-0827 cells (Figure 2A). Importantly, the protein expression levels of the ΔF-box and ΔKelch versions were similar to expression of the full-length version (Figure 2B), indicating that the difference was not simply due to insufficient expression of the ΔF-box and ΔKelch proteins. These data suggest that both the F-box domain and the Kelch domain are required for survival of F42L-*S* cells, which supports the idea that FBXO42's role in an E3 ubiquitin ligase complex is responsible for the observed phenotype.

Building upon this idea, we next wanted to know whether a known target of FBXO42 is responsible for the viability phenotype. In this scenario, knocking out the target should rescue the viability loss seen with *FBXO42* knockout in F42L-*S* cells. There are three published targets of FBXO42, including TP53 (20,21), ING4 (23) (a chromatin reader) and RBPJ (38) (a transcriptional regulator important in Notch signaling). We performed knockout rescue experiments, whereby RNPs containing *FBXO42* or control sgRNAs were co-nucleofected with sgRNAs targeting *TP53*, *ING4* and *RBPJ*. Co-nucleofections do not diminish the effect of each targeting in our conditions (35). However, as shown from representative micrographs shown in Figure 2C, knockout of these targets was not essential in GSC-0827 cells and they also failed to rescue the F42L-*S* phenotype. Figure 2D shows quantification of viability effects for each of these purported targets using a Dox-*FBXO42* GSC-0827 system, along with protein expression for each target after knockout (Figure 2E). Again, these results shows that none of these targets, when suppressed, rescues the F42L-*S* phenotype.

Of these targets, one group reported that FBXO42 directly interacts with p53 to cause its ubiquitination and degradation. They argued that loss of FBXO42 causes p53 stabilization, leading to G1 cell cycle arrest and apoptosis (20,21). Because of the importance of this possibility, we wanted to further test whether FBXO42 could be regulating p53 in p53wt F42L-*R* and F42L-*S* cells. We assessed steady-state p53 protein levels in NSCs (p53wt), which we had nucleofected with CRISPR RNPs targeting *FBXO42*, as well as in our Dox-*FBXO42*-inducible clones 6 and 15 of F42L-*S* GSC-0827 cells (Figure 2F and G). However, we did not observe any increase in steady-state levels of p53.

Furthermore, we reasoned that if the negative effect on viability observed with *FBXO42* loss were indeed due to stabilization of p53, then *TP53*-mutant cancer cell lines should be less likely to be sensitive to *FBXO42* loss than *TP53wt* cell lines. To address this, we examined the relationship between *FBXO42* dependency, *TP53* dependency and *TP53* mutation status among cancer cell lines from Figure 1C (Figure 2H). With regard to *TP53* status versus *TP53* gene effect score, the *TP53wt* cell lines tend to show positive effect scores due to enhancement of proliferation. However, the results clearly show that *FBOX42* requirement does not depend on *TP53* status, where a similar percentage of F42L-*S* cells are found in both categories. If *FBXO42* requirement were dependent on p53 status (e.g. similarly to *MDM2*), there should be a strong negative trend among TP53wt cell lines, which is not at all apparent (Figure 2H).

Taken together, our data suggest that FBXO42's role in SCF is responsible for its viability requirement in F42L-*S* cells, but that the effect is likely mediated through one or more, as yet unidentified, substrates. Moreover, the results demonstrate that p53 is not a significant target of FBXO42.

CCDC6 requirement is associated with FBXO42 requirement in F42L-*S* cells

To identify candidate protein interactors of FBXO42, we examined protein–protein interactions found in large-scale mass spectrometry-based databases, which incorporated FBXO42 (39,40). We found several known interactors, including CUL1, SKP1 and RBPJ, and a few novel candidates, including CCDC6, PPP4C and PPP4R1 (Supplementary Figure S2A). To determine relevance, we examined requirement for these among cancer cell lines showing requirement for *FBXO42*. Only one showed a significant correlation with *FBXO42* requirement: *CCDC6* (Supplementary Figure S2B).

CCDC6 is a coiled-coil domain-containing protein that is considered a tumor suppressor and was first identified due to its involvement in chromosomal rearrangements with the RET proto-oncogene in thyroid papillary carcinomas (41). It is a pro-apoptotic protein substrate of ATM that has been shown to be involved in the DNA damage response (42–44). However, *FBXO42* KO did not affect steady-state levels of CCDC6 (Supplementary Figure S2C), suggesting that it is not a *degradation* target of FBXO42.

We next assessed relative cell viability after nucleofecting two F42L-*S* lines GSC-0827 and BT549 and the two F42L-*R* lines with CRISPR RNPs targeting *FBXO42* or *CCDC6* individually or both in combination (Supplementary Figure S2D). The results confirmed that *CCDC6* dependency is associated with *FBXO42* dependency in our system as well, since *CCDC6* knockout reduced viability in GSC-0827 and BT549 but had no effect in GSC-0131 or NSC-U5. Combined loss of *FBXO42* and *CCDC6* may have a greater impact on viability in F42L-*S* cells than loss of either gene alone; however, due to the limitations of the assay and viability effects, epistasis remains a possibility (Supplementary Figure S2D–F). For F42L-*R* cells, single or combined loss of either gene did not negatively affect their outgrowth. These results indicate that F42L-*S* cells require both genes for survival, that *FBXO42* and *CCDC6* are not synthetic lethal and that CCDC6 likely participates in FBXO42 function in F42L-*S* cells.

FBXO42 loss triggers an extended mitotic arrest with misaligned chromosomes in F42L-*S* cells

We next wanted to gain insight into the cause of *FBXO42* dependency in F42L-*S* cells. Since many E3 ubiquitin ligases are involved in cell cycle control, we first determined changes in gene expression. If cells were arrested in a specific part of the cell cycle, we would expect to see a dramatic increase in cell cycle genes peaking in that phase [e.g. (45)]. Therefore, we examined gene expression changes induced by *FBXO42* loss in F42L-*S* and F42L-*R* cells. Figure 3A shows that in F42L-*R* NSCs only five genes showed significant differences (>1.5-fold increased: *APSN*, *B3GALT2* and *FABP7*; >1.5-fold decreased: *FBXO42* and *HTRA3*), while in F42L-*S* GSC-0827 cells significant changes were observed in ∼523 genes (Supplementary Table S2). For the 399 genes upregulated, there was significant enrichment for genes whose expression peaks in G2/M, including those involved in chromosome segregation and mitosis, such as *BUB1B*, *CCNB1*, *CDC20*, *CENPE*, *GTSE1* and *PLK1* (46) (Figure 3B and Supplementary Table S3).

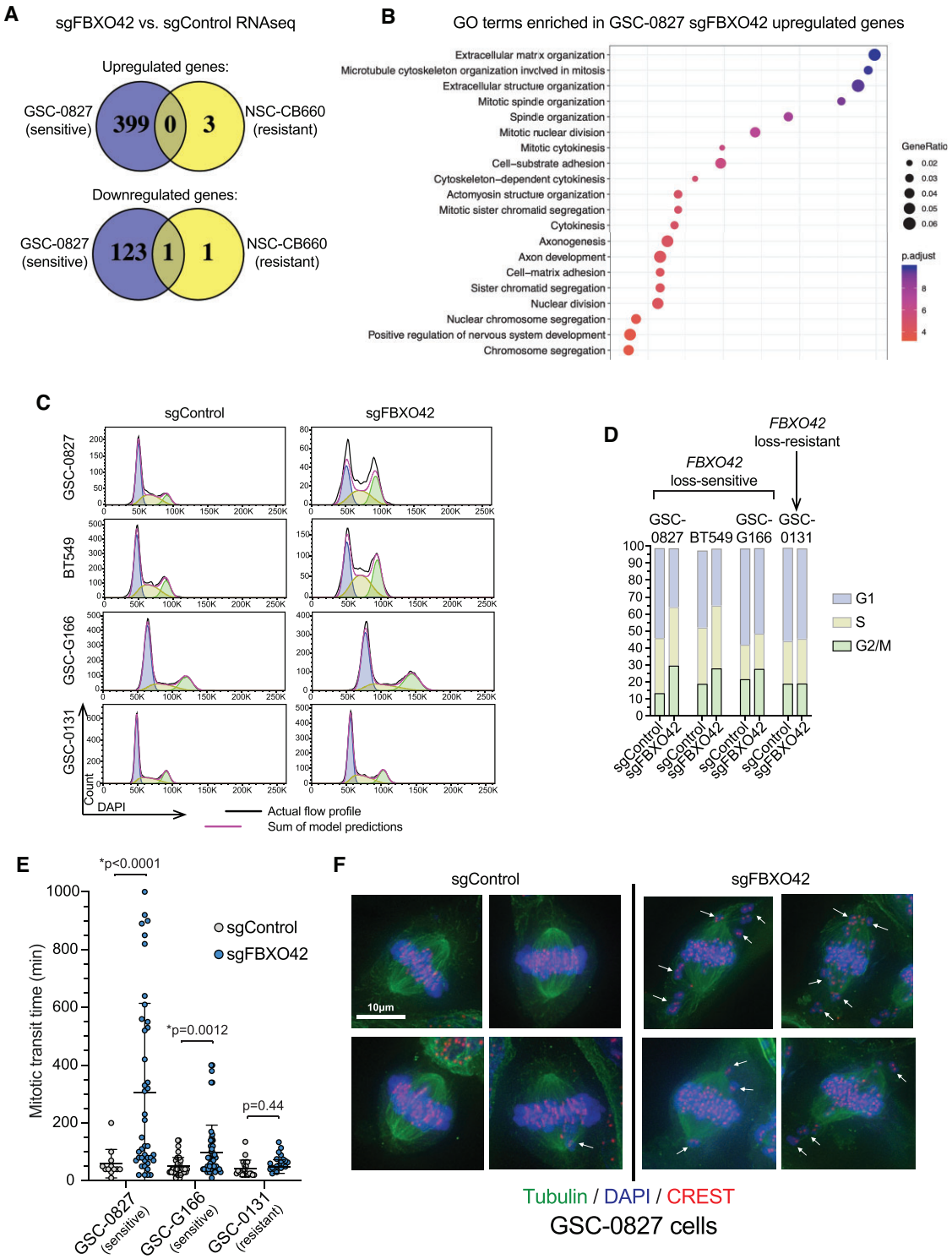

Figure 3. *FBXO42* loss triggers an extended mitotic arrest associated with misalignment of chromosomes in metaphase in F42L-*S* cells. (**A**) Comparison of gene expression changes after knockout of *FBXO42* in GSC-0827 and NSC-CB660 cells ($n = 3$; 4 days post-nucleofection). The cutoffs used for gene lists were false discovery rate <0.05 and ±1.5-fold change from the DESeq2 analysis. Supplementary Table S2 contains the full results of RNA-seq dataset and comparisons. (**B**) Gene set enrichment analysis of genes upregulated after *FBXO42* knockout in GSC-0827 cells. (**C**) DNA content (DAPI) flow cytometry profiles for cells nucleofected with CRISPR RNPs targeting *FBXO42* compared to a nontargeting sgRNA (*sgNTC*) (4 days post-nucleofection). A Dean–Jett–Fox model for cell cycle distribution (FlowJo software) is shown under the histogram for each sample, with predictions for G1, S and G2/M. (**D**) Cell cycle proportion of DNA content (DAPI) flow cytometry profiles for cells nucleofected with CRISPR RNPs targeting *FBXO42* compared to a nontargeting sgRNA (*sgNTC*) from panel (C). (**E**) Mitotic transit time, measured using analysis of time-lapse microscopy, for individual H2B-EGFP-expressing cells with or without knockout of *FBXO42*, as in panel (A). Bars show mean and standard deviation. An asterisk indicates significance as shown, Student's *t*-test. Comparisons were between sgControl and sgFBXO42 for individual GSCs. Each dot is a measurement of a single cell's mitotic transit time from multiple culture wells. (**F**) Chromosome alignment assays in *FBXO42* knockout and control GSC-0827 cells 4 days post-nucleofection were treated by 10 μM MG-132 for 2 h to arrest them at metaphase and then fixed, stained as indicated (CREST anti-serum stains human kinetochores) and visualized using deconvolution microscopy. Scale bar indicates 10 μm.

These results suggested that *FBXO42* loss in F42L-*S* cells triggers a G2/M- or M-phase cell cycle arrest. We thereby assessed the cell cycle profiles of F42L-*S* and F42L-*R* cells with and without *FBXO42* knockout using flow cytometry DNA content analysis via DAPI staining (Figure 3C). There was a marked increase in the percent of cells in the G2/M stage in F42L-*S* cells treated with *sgFBXO42*, with a concomitant decrease in the percent in G1 (Figure 3C and D). The degree of F42L sensitivity was also associated with the increase in the percent of cells observed in G2/M, as the exquisitely sensitive lines GSC-0827 and BT549 displayed the largest increase, while the moderately sensitive line GSC-G166 displayed a lesser increase. Importantly, there was no difference in cell cycle profile upon *FBXO42* loss in the F42L-resistant line GSC-0131 (Figure 3D).

Since it is not possible to distinguish between cells in G2 and M phases when using a DAPI DNA content profile to assess cell cycle, we used time-lapse microscopy in GSCs that had been transduced with a PGK-H2B-EGFP construct to determine whether we could see an effect on mitosis in *FBXO42* knockout cells (Figure 3E). We imaged cells (phase and GFP) every 5 min to compile time-lapse videos and then assessed the mitotic transit time for individual cells. We found that F42L-*S* cells with *FBXO42* knockout spent a significantly longer time in mitosis. Once again, the difference was associated with the degree of F42L sensitivity, with GSC-0827 sgFBXO42 cells spending an average of ∼3.1 times as long in mitosis as control cells (up to a maximum of ∼8.9 times) and GSC-G166 *sgFBXO42* cells spending an average of ∼1.50 times as long in mitosis as control cells (up to a maximum of ∼4.9 times) (Figure 3E). We also observed that GSC-0827 cells failed to adapt to their mitotic arrest and eventually suffered cell death during this arrest, while GSC-G166 cells were eventually able to overcome the arrest and exit mitosis. As expected, based on the flow cytometry results, there was no significant difference in mitotic transit time between *sgFBXO42* and control cells for the F42L-*R* isolate GSC-0131 (Figure 3E).

We observed from our time-lapse microscopy that the mitotic arrest seemed to be specifically a metaphase arrest, since we could see a formed metaphase plate in the arrested cells (visualized by H2B-EGFP). We wanted to explore this further and thus fixed *sgFBXO42* and control GSC-0827 cells, stained with DAPI and tubulin- and centromere-specific antibodies, and performed Z-stack ultra-high-resolution microscopy to create 3D projections of mitotic cells (Figure 3F). This confirmed that arrested cells were indeed at metaphase, and it showed that *sgFBXO42* cells suffer from both a distorted spindle and a dramatic increase in chromosome alignment defects, with many misaligned chromosomes present at the spindle poles (Figure 3F).

Altogether, these results indicate that loss of *FBXO42* in F42L-*S* cells leads to a prolonged mitosis, likely due to defects in chromosome congression and alignment.

Inhibition of SAC kinase Mps1 suppresses mitotic arrest, but not viability loss, triggered by *FBXO42* inactivation in F42L-*S* cells

A metaphase arrest triggered by misaligned chromosomes would be predicted to activate the SAC, which is a feedback control system in eukaryotic cells that monitors the attachment of kinetochores to the microtubule fibers of the mitotic spindle (47). Sister chromatids that do not have proper bi-oriented attachments at kinetochores cause SAC signaling, activating the SAC effector, the mitotic checkpoint complex (MCC) (47). The MCC binds and inhibits APC/C-Cdc20, which is required for the metaphase–anaphase transition, thus preventing entry into anaphase. In this manner, the SAC serves to prevent premature chromosome segregation in the presence of chromosomes that are not properly attached to the spindle, thereby preserving the genome from the disastrous consequences that aneuploidy can bring (48). The activity of the Mps1 kinase is required to activate the SAC by phosphorylating the kinetochore protein Knl1 (49–51), creating docking sites for the recruitment of additional SAC proteins (52–58). Its chemical inhibition prevents activation of the SAC.

To determine whether SAC activation was the cause of the prolonged metaphase arrest in F42L-*S* cells, we asked whether a brief treatment with an Mps1 inhibitor alleviates the mitotic arrest triggered by loss of *FBXO42*. To this end, we used the Dox-inducible *FBXO42* GSC-0827 cells. These cells are engineered to express the *FBXO42* ORF from the Dox-controlled tetO7 promoter to complement disruption of endogenous *FBXO42* locus when Dox is present in media (see the 'Materials and methods' section; Figure 4A). We identified outgrown clones that recapitulated loss of *FBXO42* in the absence of Dox, with demonstrable mutations in FBXO42 (Figure 4B), loss of FBXO42 protein expression after 4 days of Dox removal (Figure 4C) and reproduction of the F42L-*S* phenotype (Figure 4D). Figure 4D shows time-lapse images of mitotic arrest phenotype after Dox withdrawal for clone 15, showing profound and prolonged mitotic arrest followed by eventual loss of cell viability (see also videos in Supplementary data).

We cultured cells with or without Dox for 4 days and then treated these cells with either Mps1 inhibitor or vehicle control for 2 h and performed flow cytometry for DAPI and phospho-histone H3 (Ser10) to mark mitotic cells (Figure 4E). From the vehicle controls, we could see that at this time point >30% of cells in the Dox− condition (*FBXO42* loss) were arrested in mitosis, compared to the steady-state level of 2.25% in the Dox+ control (Figure 4F). After treatment with Mps1 inhibition, only 3.8% of cells were in mitosis in the Dox− condition, indicating that Mps1 activity is required for the mitotic arrest phenotype (Figure 4F).

We also assessed the relative cell viability in cells cultured with or without Dox and with or without Mps1 inhibition (Figure 4G). Although there was a partial rescue of viability in the presence of the inhibitor, overall the cells still lost viability after treatment (Figure 4G). This likely indicates that chromosome segregation errors caused by loss of *FBXO42* are of sufficient magnitude to cause significant loss of viability, regardless of SAC activation. We conclude that the mechanism of cancer-specific requirement of *FBXO42* is to promote congression and kinetochore–microtubule attachment and prevent triggering of the SAC.

FBXO42 inactivation compromises F42L-*S* GSC tumor growth

Next, we wished to determine whether the F42L-*S* phenotype holds true *in vivo* in GSC-derived tumors. We used the Dox-inducible *FBXO42* GSC-0827 cells (clone 15) described above. To ensure that Dox would be bioavailable to tumor cells, we used a flank tumor model to evaluate effect of *FBXO42* loss after tumors had already formed (Figure 5A).

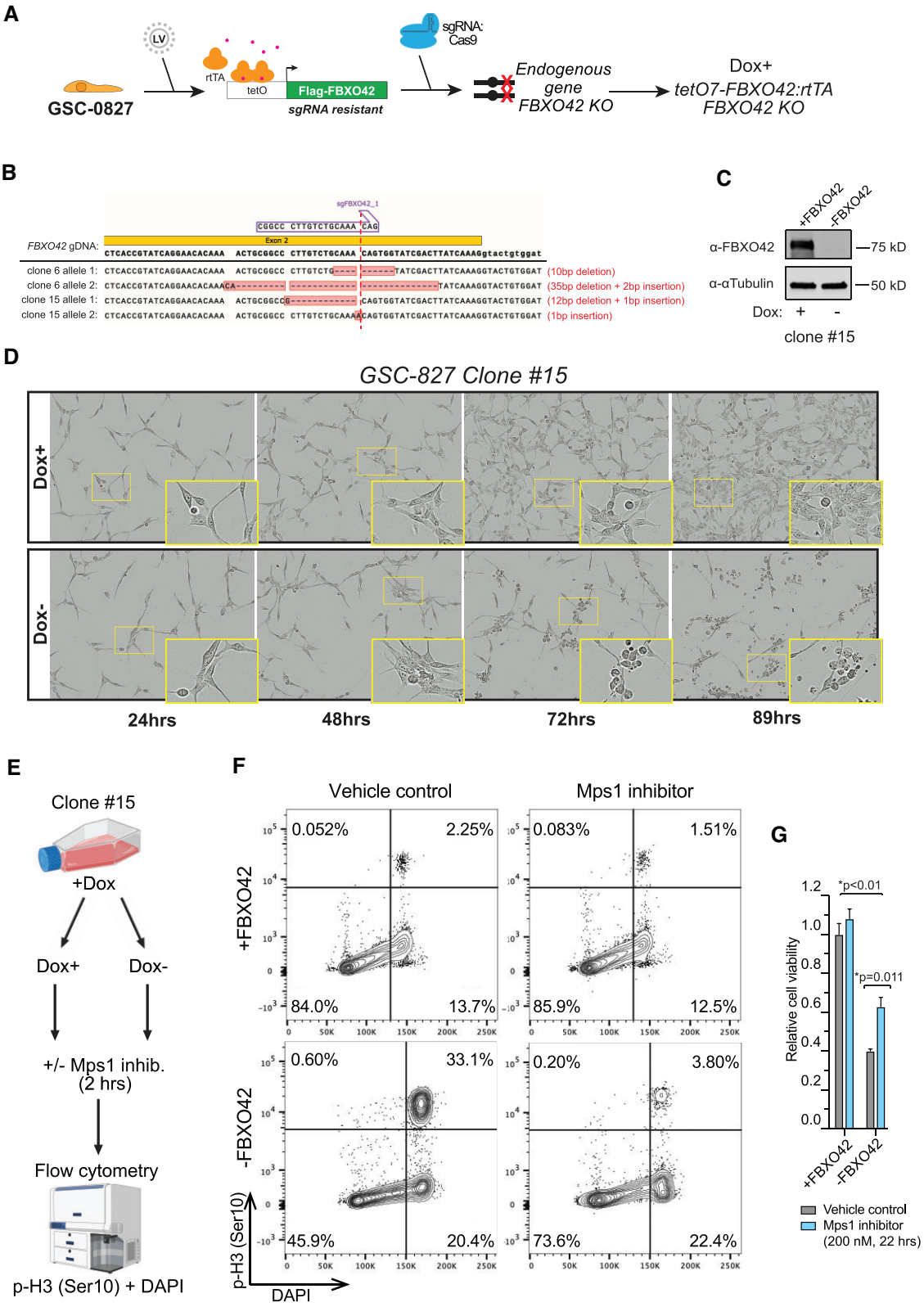

Figure 4. Inhibition of SAC kinase Mps1 bypasses G2/M arrest, but not loss of viability, triggered by *FBXO42* inactivation in F42L-*S* cells. (**A**) Overview of creation of Dox controllable *FBXO42* cells. (**B**) Indel analysis of endogenous *FBXO42* locus of two GSC-0827 clones. (**C**) Western blot for FBXO42 for clone 15 with either continuous Dox exposure or 4 days after Dox removal. Clone 15 cells harbor a biallelic disruption of endogenous *FBXO42* locus and also express a Dox-controlled *FBXO42* ORF, which complements the loss of endogenous *FBXO42*. (**D**) Photomicrographs taken from time-lapse videos of clone 15 cells grown with and without Dox (times after Dox withdrawal are indicated) (see videos in Supplementary data for full dataset). (**E**) Overview of experiment performed in panel (F). (**F**) DAPI versus phospho-histone H3 (Ser10) flow cytometry profiles for GSC-0827 Dox-inducible *FBXO42* clone 15 kept in ±Dox for 4 days and then treated with vehicle or an Mps1 inhibitor (NMS-P715) for 2 h. (**G**) Relative viability for cells that were kept in ±Dox for 4 days and then treated with vehicle or 200 nM Mps1 inhibitor for 22 h ($n = 3$; $^{*}P_{val} < 0.01$, Student's *t*-test).

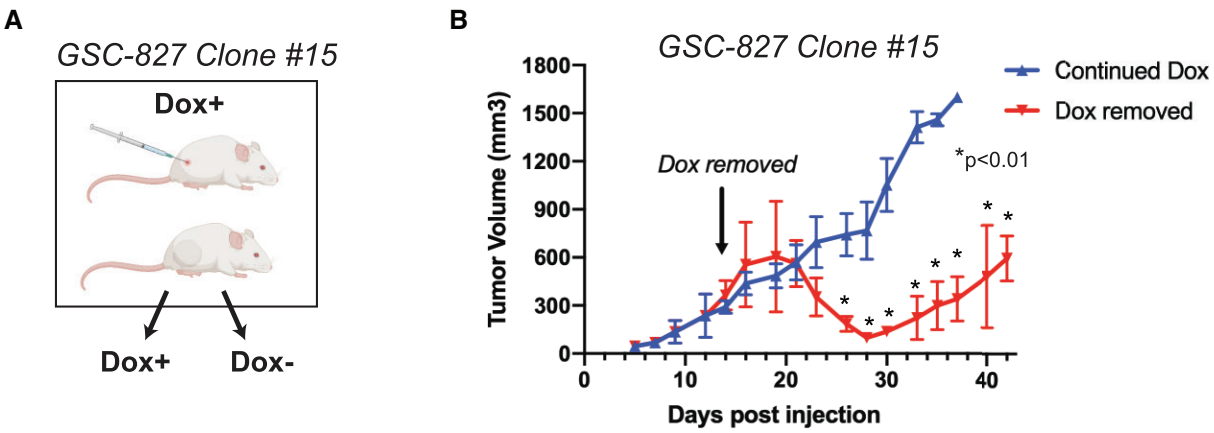

Figure 5. Growth of tumors derived from F42L-*S* cells is inhibited by loss of FBXO42. (**A**) Tumor growth of GSC-0827 Dox-*FBXO42* clone 15 cells with and without Dox. (**B**) Flank tumors ($n = 5$ for each arm; $^{*}P_{val} < 0.01$, two-way analysis of variance) were used to avoid any potential bioavailability issues with Dox crossing the blood–brain barrier.

We observe that after attenuating *FBXO42* expression via Dox removal, GSC-0827 tumors show a substantial loss in tumor volume, almost becoming undetectable, before gradually regrowing (Figure 5B). The results suggest that *FBXO42* is requirement for maintenance of tumor growth in F42L-*S* cells.

Discussion

Here, we characterized cancer-specific requirement for the F-box protein encoding gene *FBXO42*. Starting with GBM isolates, we found a novel viability requirement in ∼15% of cancer cell lines that seems independent of tissue of origin (Figure 1), which was also observed in patient-derived xenograft tumors. In F42L-*S* cells, *FBXO42* was required to prevent mitotic delay or extended arrest driven by SAC activation. We observed that FBXO42's F-box and Kelch domains were critical to maintaining viability of F42L-*S* cells, implicating its SCF-associated ubiquitin ligase activity. However, none of FBXO42's known substrates were required, as deleting them had no effect on *FBXO42* loss phenotype. In contrast to two previous reports, we also show that FBXO42 does not affect steady-state p53 levels or modulate cell growth of p53wt in a manner consistent with p53 being a degradation target. Instead, we propose a model of *FBXO42* requirement in which FBXO42 facilitates degradation of a novel cancer-specific target in F42L-*S* cells (Figure 6). In the absence of FBXO42 activity, the degradation target accumulates and perturbs chromosome–spindle dynamics, triggering spindle assembly checking arrest and ultimately cell death.

A recent study examining roles for E3 ubiquitin ligase complex genes in broad range of biological processes, including cell cycle modulatory drugs, identified *FBXO42*-mutant cells as being sensitive to mitotic inhibitors, including BI-2536 (Plk1) and colchicine (microtubules) (24). They were further able to show that in *FBXO42*-mutant HAP1 cells, there was an increased frequency of monopolar spindles upon BI-2536 treatment. While they were not able to establish a mechanism, the results suggest that FBXO42 activity helps buffer the effects of perturbations in chromosome–spindle dynamics. Given these results along with our own, it is likely that *FBXO42* requirement in F42L-*S* cells is caused by an underlying perturbation in chromosome–spindle dynamics.

Consistent with this notion, we observed chromosome alignment defects in sensitive GSC-0827 cells, which is the classic cause of SAC activation [reviewed in (59)]. In addition, we also observed that the mitotic spindle was noticeably twisted and distorted (Figure 3F). Therefore, it is also possible that FBXO42 substrate(s) act on the mitotic spindle and thereby cause prolonged activation of the SAC (60).

For GBM isolates, we have previously established that there are at least two cancer-specific defects in kinetochore–microtubule dynamics that can cause profound loss of chromosome–spindle attachments (47). The most dramatic of these is caused by inappropriate Ras/MAP kinase activity in mitosis (12,13,19). About half of GBM isolates tested suffer from this defect, which causes a characteristic change in sister kinetochore morphology and a novel dependence for BUB1B/BubR1 (12,19). However, F42L-*S* GSC-0827 cells do not have this kinetochore defect (19). Thus, *FBXO42* requirement represents a separate and novel form of mitotic perturbation. Identifying its key mitotic-relevant substrate(s) will likely be key to understanding the mechanism of its cancer-specific requirement.

However, we were unable to identify FBXO42's relevant substrate(s) for the phenotypes reported above, either from those published or from the ones we attempted to identify by immunoprecipitation–mass spectrometry (data not shown). This includes p53, which has been proposed to be key substrate of FBXO42, where FBXO42 acts through the SCF complex to destabilize baseline p53 levels similarly to MDM2 (20,21). In fact, because GSC-0827 cells are p53wt (i.e. by exome sequencing), we initially assumed that their FBXO42 viability requirement would arise via p53 stabilization and arrest or apoptosis in *FBXO42*-deficient cells. However, this was not the case: we were unable to find evidence in GSC-0827 or NSC-CB660 cells for loss of *FBXO42* leading to increases in steady-state p53 levels as reported in (20,21) (Figure 2). We reasoned that this could be due to a cell-type difference. However, when examining *FBXO42* and *MDM2* requirements across hundreds of human cell lines, only *MDM2* requirement was anticorrelated with p53 mutation status. That is, *MDM2* requirement was absent or attenuated in p53mut lines, while *FBXO42* requirement was not (Figure 2H). Further, U2OS osteosarcoma cancer cells, originally used for FBXO42 studies by Sun *et al.* (21), are wt *TP53* but do not display a require-

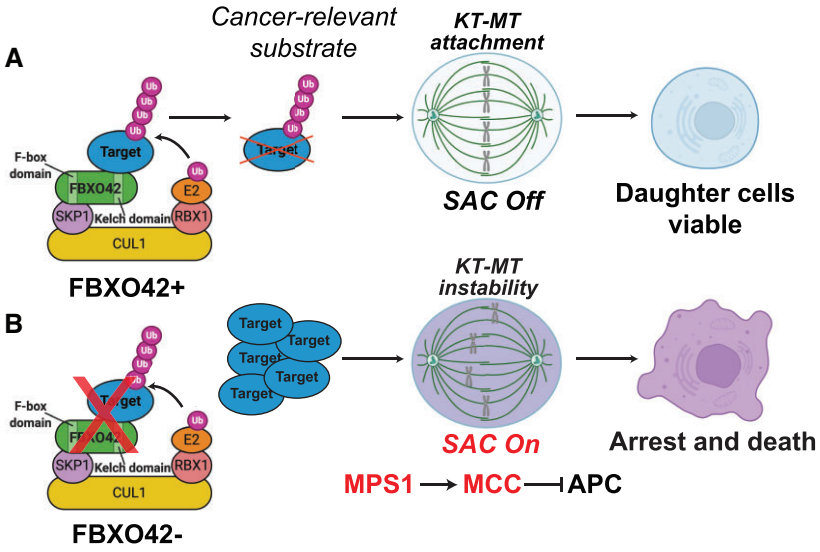

Figure 6. A model for cancer-specific requirement of *FBXO42*. (**A**) FBXO42 interacts with and regulates one or more substrates through its Kelch domain as part of SCF E3 ubiquitin ligase complex promoting chromosome–microtubule interactions and preventing SAC activation. (**B**) Loss of FBXO42 activity in sensitive cancer cells causes loss of regulation of protein target(s), perturbation of kinetochore–microtubule interactions, inhibition of anaphase, extended mitotic arrest and cell death. MCC, mitotic checkpoint complex; APC, CDC20-containing anaphase-promoting complex.

ment for *FBOX42*, while, as expected, do need *MDM2* activity (gene effect scores = −0.04 and −1.21, respectively). The original studies linking FBXO42 to p53 used ectopic overexpression of tagged *FBXO42*. It is possible that this scenario led to a nonphysiological effect altering turn over p53. Further studies focused on endogenous FBXO42 complexes and substrates will be required to address these issues.

However, we were able to confirm requirement for *CCDC6*, which appears in protein–protein interaction databases as interacting with FBXO42. *FBXO42* and *CCDC6* show strong positive correlation of requirement among human cell lines (Supplementary Figure S2B). Combined loss of *FBXO42* and *CCDC6* might have a greater impact on viability in F42L-*S* cells; however, due to the limitations of the assay, epistasis seems just as likely (Supplementary Figure S2D). CCDC6 is pro-apoptotic protein substrate of ATM that has been shown to be involved in the DNA damage response (42–44). One study has shown that its loss accelerates entry into mitosis after DNA damage through negative regulation of the PPP4C–PPP4R1 PP4 phosphatase (44). PP4 targets phosphorylated H2AX after DNA damage, which is critical for DNA repair signaling and reentry into the cell cycle (61).

Interestingly, the PPP4C–PPP4R1 PP4 phosphatase complex is found to interact with FBXO42 as well (Supplementary Figure S2A). In addition to targeting pH2AX, this complex can affect microtubule organization via negative regulation of CDK1 interphase, causing abnormal phosphorylation of NDEL1 (62), which in turn localizes to kinetochores, affects chromosome alignment and triggers SAC when inhibited (63). This would be consistent with CCDC6's role as a negative regulator of PP4 activity (44). However, this does not explain why both would be selectively required by some cancer cells and not others. One speculative possibility is that F42L-*S* cells have higher intrinsic DNA genotoxic stress, which could lead to differential sensitivity to PP4 regulation. For example, we have shown that GBM cells are hypersensitive to loss of inhibitory phosphorylation of CDK1 (16), a sensitivity shown to result from DNA replication stress (64).

However, could CCDC6 itself be the relevant target of FBXO42 in *FBXO42*-requiring cancer cells? A recent study showed that FBXO42-mediated K63-linked polyubiquitination of the transcriptional regulator RBPJ was required for RBPJ's regulation of chromatin and Notch signaling (65). K63-linked polyubiquitination does not cause proteasomal degradation, but rather modification of protein function (66). Thus, while our results are not consistent with CCDC6 being a degradation target of FBXO42, we cannot rule it out as a nonproteasomal target. In fact, the results would be consistent with this possibility. Further experiments, however, are required to examine these and other possibilities regarding *FBXO42* and *CCDC6* functions.

Data availability

The RNA-seq data that support the findings of this study are openly available in the NCBI Gene Expression Omnibus (GEO) at https://www.ncbi.nlm.nih.gov/geo/, GEO accession number GSE213269. Other data that support the findings of this study are available in Supplementary data.

Supplementary data

Supplementary Data are available at NAR Cancer Online.

Acknowledgements

We thank members of the Paddison and Olson Lab for helpful discussions, and Pam Lindberg and An Tyrrell for administrative support.

Author contributions: Project conception and design was carried out by P.H. and P.J.P.; experiments and data analysis were performed by P.H., E.J.G. and J.A.H.; critical reagents were generated by M.K.; bioinformatics data analysis and statistics were performed by P.H., S.A. and P.J.P.; manuscript was written by P.J.P. and P.H. with input from other authors; and funding acquisition was performed by J.M.O. and P.J.P.

Funding

National Cancer Institute [T32CA080416 to P.H., R01CA190957 to P.J.P., R01CA114567 to J.M.O., P30 CA015704 (in part)]; National Institute of Neurological Disorders and Stroke [R01NS119650 to P.J.P.].

Conflict of interest statement

None declared.

References

1. Goodenberger,M.L. and Jenkins,R.B. (2012) Genetics of adult glioma. *Cancer Genet.*, **205**, 613–621.
2. Louis,D.N., Ohgaki,H., Wiestler,O.D., Cavenee,W.K., Burger,P.C., Jouvet,A., Scheithauer,B.W. and Kleihues,P. (2007) The 2007 WHO classification of tumours of the central nervous system. *Acta Neuropathol.*, **114**, 97–109.
3. CBTRUS (2011) www.cbtrus.org (October 2023, date last accessed).
4. Latera,J. and Brem,H. (2002) Primary brain tumours in adults. In: Asbury,A.K., McKhann,G.M., McDonald,W.I., Goadsby,P.J. and McArthur,J.C. (eds.) *Diseases of the Nervous System: Clinical Neuroscience and Therapeutic Principles*. Vol. **2**, 3rd edn. Cambridge University Press, Cambridge, UK, pp. 1431–1466.
5. Stupp,R., Mason,W.P., van den Bent,M.J., Weller,M., Fisher,B., Taphoorn,M.J., Belanger,K., Brandes,A.A., Marosi,C., Bogdahn,U., *et al.* (2005) Radiotherapy plus concomitant and adjuvant temozolomide for glioblastoma. *N. Engl. J. Med.*, **352**, 987–996.
6. O'Reilly,S.M., Newlands,E.S., Glaser,M.G., Brampton,M., Rice-Edwards,J.M., Illingworth,R.D., Richards,P.G., Kennard,C., Colquhoun,I.R., Lewis,P., *et al.* (1993) Temozolomide: a new oral cytotoxic chemotherapeutic agent with promising activity against primary brain tumours. *Eur. J. Cancer*, **29A**, 940–942.
7. Hemmati,H.D., Nakano,I., Lazareff,J.A., Masterman-Smith,M., Geschwind,D.H., Bronner-Fraser,M. and Kornblum,H.I. (2003) Cancerous stem cells can arise from pediatric brain tumors. *Proc. Natl Acad. Sci. U.S.A.*, **100**, 15178–15183.
8. Singh,S.K., Clarke,I.D., Terasaki,M., Bonn,V.E., Hawkins,C., Squire,J. and Dirks,P.B. (2003) Identification of a cancer stem cell in human brain tumors. *Cancer Res.*, **63**, 5821–5828.
9. Lee,J., Kotliarova,S., Kotliarov,Y., Li,A., Su,Q., Donin,N.M., Pastorino,S., Purow,B.W., Christopher,N., Zhang,W., *et al.* (2006) Tumor stem cells derived from glioblastomas cultured in bFGF and EGF more closely mirror the phenotype and genotype of primary tumors than do serum-cultured cell lines. *Cancer Cell*, **9**, 391–403.
10. Chen,J., Li,Y., Yu,T.S., McKay,R.M., Burns,D.K., Kernie,S.G. and Parada,L.F. (2012) A restricted cell population propagates glioblastoma growth after chemotherapy. *Nature*, **488**, 522–526.
11. Pollard,S.M., Yoshikawa,K., Clarke,I.D., Danovi,D., Stricker,S., Russell,R., Bayani,J., Head,R., Lee,M., Bernstein,M., *et al.* (2009) Glioma stem cell lines expanded in adherent culture have tumor-specific phenotypes and are suitable for chemical and genetic screens. *Cell Stem Cell*, **4**, 568–580.
12. Ding,Y., Hubert,C.G., Herman,J., Corrin,P., Toledo,C.M., Skutt-Kakaria,K., Vazquez,J., Basom,R., Zhang,B., Risler,J.K., *et al.* (2013) Cancer-specific requirement for BUB1B/BUBR1 in human brain tumor isolates and genetically transformed cells. *Cancer Discov.*, **3**, 198–211.
13. Lee,E., Pain,M., Wang,H., Herman,J.A., Toledo,C.M., DeLuca,J.G., Yong,R.L., Paddison,P. and Zhu,J. (2017) Sensitivity to BUB1B inhibition defines an alternative classification of glioblastoma. *Cancer Res.*, **77**, 5518–5529.
14. Hubert,C.G., Bradley,R.K., Ding,Y., Toledo,C.M., Herman,J., Skutt-Kakaria,K., Girard,E.J., Davison,J., Berndt,J., Corrin,P., *et al.* (2013) Genome-wide RNAi screens in human brain tumor isolates reveal a novel viability requirement for PHF5A. *Genes Dev.*, **27**, 1032–1045.
15. Toledo,C.M., Herman,J.A., Olsen,J.B., Ding,Y., Corrin,P., Girard,E.J., Olson,J.M., Emili,A., DeLuca,J.G. and Paddison,P.J. (2014) BuGZ is required for Bub3 stability, Bub1 kinetochore function, and chromosome alignment. *Dev. Cell*, **28**, 282–294.
16. Toledo,C.M., Ding,Y., Hoellerbauer,P., Davis,R.J., Basom,R., Girard,E.J., Lee,E., Corrin,P., Hart,T., Bolouri,H., *et al.* (2015) Genome-wide CRISPR–Cas9 screens reveal loss of redundancy between PKMYT1 and WEE1 in glioblastoma stem-like cells. *Cell Rep.*, **13**, 2425–2439.
17. Ding,Y., Herman,J.A., Toledo,C.M., Lang,J.M., Corrin,P., Girard,E.J., Basom,R., Delrow,J.J., Olson,J.M. and Paddison,P.J. (2017) ZNF131 suppresses centrosome fragmentation in glioblastoma stem-like cells through regulation of HAUS5. *Oncotarget*, **8**, 48545–48562.
18. Danovi,D., Folarin,A., Gogolok,S., Ender,C., Elbatsh,A.M.O., Engström,P.G., Stricker,S.H., Gagrica,S., Georgian,A., Ding,Y., *et al.*, (2013) A high-content small molecule screen identifies sensitivity of glioblastoma stem cells to inhibition of polo-like kinase 1. *PLoS One*, **8**, e77053.
19. Herman,J.A., Romain,R.R., Hoellerbauer,P., Shirnekhi,H.K., King,D.C., DeLuca,K.F., Osborne Nishimura,E., Paddison,P.J. and DeLuca,J.G. (2022) Hyper-active RAS/MAPK introduces cancer-specific mitotic vulnerabilities. *Proc. Natl Acad. Sci. U.S.A.*, **119**, e2208255119.
20. Sun,L., Shi,L., Wang,F., Huangyang,P., Si,W., Yang,J., Yao,Z. and Shang,Y. (2011) Substrate phosphorylation and feedback regulation in JFK-promoted p53 destabilization. *J. Biol. Chem.*, **286**, 4226–4235.
21. Sun,L., Shi,L., Li,W., Yu,W., Liang,J., Zhang,H., Yang,X., Wang,Y., Li,R., Yao,X., *et al.* (2009) JFK, a Kelch domain-containing F-box protein, links the SCF complex to p53 regulation. *Proc. Natl Acad. Sci. U.S.A.*, **106**, 10195–10200.
22. Nagler,A., Vredevoogd,D.W., Alon,M., Cheng,P.F., Trabish,S., Kalaora,S., Arafeh,R., Goldin,V., Levesque,M.P., Peeper,D.S., *et al.* (2020) A genome-wide CRISPR screen identifies FBXO42 involvement in resistance toward MEK inhibition in NRAS-mutant melanoma. *Pigment Cell Melanoma Res.*, **33**, 334.
23. Yan,R., He,L., Li,Z., Han,X., Liang,J., Si,W., Chen,Z., Li,L., Xie,G., Li,W., *et al.* (2015) SCFJFK is a bona fide E3 ligase for ING4 and a potent promoter of the angiogenesis and metastasis of breast cancer. *Genes Dev.*, **29**, 672–685.
24. Hundley,F.V., Sanvisens Delgado,N., Marin,H.C., Carr,K.L., Tian,R. and Toczyski,D.P. (2021) A comprehensive phenotypic CRISPR–Cas9 screen of the ubiquitin pathway uncovers roles of ubiquitin ligases in mitosis. *Mol. Cell*, **81**, 1319–1336.
25. Sanjana,N.E., Shalem,O. and Zhang,F. (2014) Improved vectors and genome-wide libraries for CRISPR screening. *Nat. Methods*, **11**, 783–784.
26. Langmead,B., Trapnell,C., Pop,M. and Salzberg,S.L. (2009) Ultrafast and memory-efficient alignment of short DNA sequences to the human genome. *Genome Biol.*, **10**, R25.
27. Robinson,M.D., McCarthy,D.J. and Smyth,G.K. (2010) edgeR: a Bioconductor package for differential expression analysis of digital gene expression data. *Bioinformatics*, **26**, 139–140.
28. Dobin,A., Davis,C.A., Schlesinger,F., Drenkow,J., Zaleski,C., Jha,S., Batut,P., Chaisson,M. and Gingeras,T.R. (2013) STAR: ultrafast universal RNA-seq aligner. *Bioinformatics*, **29**, 15–21.
29. Anders,S., Pyl,P.T. and Huber,W. (2015) HTSeq—a Python framework to work with high-throughput sequencing data. *Bioinformatics*, **31**, 166–169.
30. Wickham,H. and Sievert,C. (2016) In: *ggplot2: Elegant Graphics for Data Analysis*. Springer International Publishing AG, Cham, Switzerland.
31. Kolde,R. (2018) pheatmap: pretty heatmaps. R package version 1.0.10. https://CRAN.R-project.org/package=pheatmap (May 2021, date last accessed).
32. Hsiau,T., Conant,D., Maures,T., Waite,K., Yang,J., Kelso,R., Holden,K., Enzmann,B.L. and Stoner,R. (2022) Inference of CRISPR edits from Sanger trace data. *CRISPR J.*, **5**, 123–130.

33. Meyers,R.M., Bryan,J.G., McFarland,J.M., Weir,B.A., Sizemore,A.E., Xu,H., Dharia,N.V., Montgomery,P.G., Cowley,G.S., Pantel,S., *et al.* (2017) Computational correction of copy number effect improves specificity of CRISPR–Cas9 essentiality screens in cancer cells. *Nat. Genet.*, **49**, 1779–1784.
34. Behan,F.M., Iorio,F., Picco,G., Goncalves,E., Beaver,C.M., Migliardi,G., Santos,R., Rao,Y., Sassi,F., Pinnelli,M., *et al.* (2019) Prioritization of cancer therapeutic targets using CRISPR–Cas9 screens. *Nature*, **568**, 511–516.
35. Hoellerbauer,P., K.M.,A.S., Wu,H., Feldman,H.M. and Paddison,P. (2020) A simple and highly efficient method for multi-allelic CRISPR–Cas9 editing in primary cell cultures. *Cancer Rep.*, **3**, e1269.
36. Sun,L., Shi,L., Li,W., Yu,W., Liang,J., Zhang,H., Yang,X., Wang,Y., Li,R., Yao,X., *et al.* (2009) JFK, a Kelch domain-containing F-box protein, links the SCF complex to p53 regulation. *Proc. Natl Acad. Sci. U.S.A.*, **106**, 10195–10200.
37. Jin,J., Cardozo,T., Lovering,R.C., Elledge,S.J., Pagano,M. and Harper,J.W. (2004) Systematic analysis and nomenclature of mammalian F-box proteins. *Genes Dev.*, **18**, 2573–2580.
38. Li,X., Wang,W., Wang,J., Malovannaya,A., Xi,Y., Li,W., Guerra,R., Hawke,D.H., Qin,J. and Chen,J. (2015) Proteomic analyses reveal distinct chromatin-associated and soluble transcription factor complexes. *Mol. Syst. Biol.*, **11**, 775–775.
39. Schweppe,D.K., Huttlin,E.L., Harper,J.W. and Gygi,S.P. (2018) BioPlex Display: an interactive suite for large-scale AP–MS protein–protein interaction data. *J. Proteome Res.*, **17**, 722–726.
40. Huttlin,E.L., Bruckner,R.J., Paulo,J.A., Cannon,J.R., Ting,L., Baltier,K., Colby,G., Gebreab,F., Gygi,M.P., Parzen,H., *et al.* (2017) Architecture of the human interactome defines protein communities and disease networks. *Nature*, **545**, 505–509.
41. Pierotti,M.A., Santoro,M., Jenkins,R.B., Sozzi,G., Bongarzone,I., Grieco,M., Monzini,N., Miozzo,M., Herrmann,M.A. and Fusco,A. (1992) Characterization of an inversion on the long arm of chromosome 10 juxtaposing D10S170 and RET and creating the oncogenic sequence RET/PTC. *Proc. Natl Acad. Sci. U.S.A.*, **89**, 1616–1620.
42. Merolla,F., Pentimalli,F., Pacelli,R., Vecchio,G., Fusco,A., Grieco,M. and Celetti,A. (2007) Involvement of H4(D10S170) protein in ATM-dependent response to DNA damage. *Oncogene*, **26**, 6167–6175.
43. JunGang,Z., Jun,T., WanFu,M. and KaiMing,R. (2012) FBXW7-mediated degradation of CCDC6 is impaired by ATM during DNA damage response in lung cancer cells. *FEBS Lett.*, **586**, 4257–4263.
44. Merolla,F., Luise,C., Muller,M.T., Pacelli,R., Fusco,A. and Celetti,A. (2012) Loss of CCDC6, the first identified RET partner gene, affects pH2AX S139 levels and accelerates mitotic entry upon DNA damage. *PLoS One*, **7**, e36177.
45. Whitfield,M.L., Sherlock,G., Saldanha,A.J., Murray,J.I., Ball,C.A., Alexander,K.E., Matese,J.C., Perou,C.M., Hurt,M.M., Brown,P.O., *et al.* (2002) Identification of genes periodically expressed in the human cell cycle and their expression in tumors. *Mol. Biol. Cell*, **13**, 1977–2000.
46. Santos,A., Wernersson,R. and Jensen,L.J. (2015) Cyclebase 3.0: a multi-organism database on cell-cycle regulation and phenotypes. *Nucleic Acids Res.*, **43**, D1140–D1144.
47. Herman,J.A., Toledo,C.M., Olson,J.M., DeLuca,J.G. and Paddison,P.J. (2015) Molecular pathways: regulation and targeting of kinetochore–microtubule attachment in cancer. *Clin. Cancer Res.*, **21**, 233–239.
48. Santaguida,S. and Amon,A. (2015) Short- and long-term effects of chromosome mis-segregation and aneuploidy. *Nat. Rev. Mol. Cell Biol.*, **16**, 473–485.
49. Yamagishi,Y., Yang,C.-H., Tanno,Y. and Watanabe,Y. (2012) MPS1/Mph1 phosphorylates the kinetochore protein KNL1/Spc7 to recruit SAC components. *Nat. Cell Biol.*, **14**, 746–752.
50. London,N., Ceto,S., Ranish,J.A. and Biggins,S. (2012) Phosphoregulation of Spc105 by Mps1 and PP1 regulates Bub1 localization to kinetochores. *Curr. Biol.*, **22**, 900–906.
51. Shepperd,L.A., Meadows,J.C., Sochaj,A.M., Lancaster,T.C., Zou,J., Buttrick,G.J., Rappsilber,J., Hardwick,K.G. and Millar,J.B.A. (2012) Phosphodependent recruitment of Bub1 and Bub3 to Spc7/KNL1 by Mph1 kinase maintains the spindle checkpoint. *Curr. Biol.*, **22**, 891–899.
52. Zhang,G., Lischetti,T. and Nilsson,J. (2014) A minimal number of MELT repeats supports all the functions of KNL1 in chromosome segregation. *J. Cell Sci.*, **127**, 871.
53. Lischetti,T., Zhang,G., Sedgwick,G.G., Bolanos-Garcia,V.M. and Nilsson,J. (2014) The internal Cdc20 binding site in BubR1 facilitates both spindle assembly checkpoint signalling and silencing. *Nat. Commun.*, **5**, 5563.
54. Primorac,I., Weir,J.R., Chiroli,E., Gross,F., Hoffmann,I., van Gerwen,S., Ciliberto,A. and Musacchio,A. (2013) Bub3 reads phosphorylated MELT repeats to promote spindle assembly checkpoint signaling. *eLife*, **2**, e01030.
55. Moyle,M.W., Kim,T., Hattersley,N., Espeut,J., Cheerambathur,D.K., Oegema,K. and Desai,A. (2014) A Bub1–Mad1 interaction targets the Mad1–Mad2 complex to unattached kinetochores to initiate the spindle checkpoint. *J. Cell Biol.*, **204**, 647–657.
56. Vleugel,M., Omerzu,M., Groenewold,V., Hadders,M.A., Lens,S.M.A. and Kops,G.J.P.L. (2015) Sequential multisite phospho-regulation of KNL1–BUB3 interfaces at mitotic kinetochores. *Mol. Cell*, **57**, 824–835.
57. Vleugel,M., Tromer,E., Omerzu,M., Groenewold,V., Nijenhuis,W., Snel,B. and Kops,G.J.P.L. (2013) Arrayed BUB recruitment modules in the kinetochore scaffold KNL1 promote accurate chromosome segregation. *J. Cell Biol.*, **203**, 943–955.
58. Krenn,V., Overlack,K., Primorac,I., van Gerwen,S. and Musacchio,A. (2014) KI motifs of human Knl1 enhance assembly of comprehensive spindle checkpoint complexes around MELT repeats. *Curr. Biol.*, **24**, 29–39.
59. Musacchio,A. (2015) The molecular biology of spindle assembly checkpoint signaling dynamics. *Curr. Biol.*, **25**, R1002–R1018.
60. Matson,D.R. and Stukenberg,P.T. (2011) Spindle poisons and cell fate: a tale of two pathways. *Mol. Interv.*, **11**, 141–150.
61. Fernandez-Capetillo,O., Lee,A., Nussenzweig,M. and Nussenzweig,A. (2004) H2AX: the histone guardian of the genome. *DNA Repair (Amst.)*, **3**, 959–967.
62. Toyo-oka,K., Mori,D., Yano,Y., Shiota,M., Iwao,H., Goto,H., Inagaki,M., Hiraiwa,N., Muramatsu,M., Wynshaw-Boris,A., *et al.* (2008) Protein phosphatase 4 catalytic subunit regulates Cdk1 activity and microtubule organization via NDEL1 dephosphorylation. *J. Cell Biol.*, **180**, 1133–1147.
63. Vergnolle,M.A. and Taylor,S.S. (2007) Cenp-F links kinetochores to Ndel1/Nde1/Lis1/dynein microtubule motor complexes. *Curr. Biol.*, **17**, 1173–1179.
64. Diab,A., Gem,H., Swanger,J., Kim,H.Y., Smith,K., Zou,G., Raju,S., Kao,M., Fitzgibbon,M., Loeb,K.R., *et al.* (2020) FOXM1 drives HPV+ HNSCC sensitivity to WEE1 inhibition. *Proc. Natl Acad. Sci. U.S.A.*, **117**, 28287–28296.
65. Jiang,H., Bian,W., Sui,Y., Li,H., Zhao,H., Wang,W. and Li,X. (2022) FBXO42 facilitates Notch signaling activation and global chromatin relaxation by promoting K63-linked polyubiquitination of RBPJ. *Sci. Adv.*, **8**, eabq4831.
66. Nathan,J.A., Kim,H.T., Ting,L., Gygi,S.P. and Goldberg,A.L. (2013) Why do cellular proteins linked to K63-polyubiquitin chains not associate with proteasomes? *EMBO J.*, **32**, 552–565.

Received: March 12, 2024. **Revised:** April 23, 2024. **Editorial Decision:** April 25, 2024. **Accepted:** May 15, 2024